

Temperature-regulating Phase Change Fiber Scaffold towards Mild Photothermal-chemotherapy

Lei Chen^a, Xiaoqing Sun^a, Kai Cheng^a, Paul D. Topham^b, Mengmeng Xu^a, Yifan Jia^a,
Donghua Dong^a, Shuo Wang^a, Yuan Liu^a, Linge Wang^{a,*}, Qianqian Yu^{a,*}

^a South China Advanced Institute for Soft Matter Science and Technology, School of Emergent Soft Matter, Guangdong Provincial Key Laboratory of Functional and Intelligent Hybrid Materials and Devices, South China University of Technology, Guangzhou, 510640, China.

^b Chemical Engineering and Applied Chemistry, School of Infrastructure and Sustainable Engineering, College of Engineering and Physical Sciences, Aston University, Birmingham, B4 7ET, UK.

Abstract

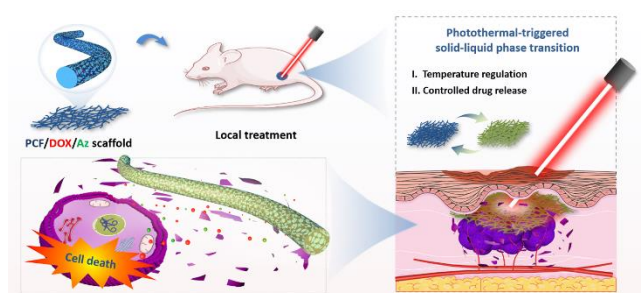
Photothermal therapy (PTT) is a treatment that raises the temperature of tumors to 42-48°C, or even higher for tumor ablation. PTT has sparked a lot of attention due to its ability to induce apoptosis or increase sensitivity to chemotherapy. Excessive heat kills tumor cells but also causes harm to surrounding healthy tissue, reducing therapeutic accuracy and increasing side effects. Herein, a phase change fiber (PCF) scaffold that acts as a thermal trigger in mild photothermal-chemo tumor therapy is developed to regulate temperature and control drug release. These prepared PCFs, comprised of hollow carbon fibers (HCFs) loaded with lauric acid as a phase change material (PCM),

can effectively store and release any excess heat generated by irradiating with a near-infrared (NIR) laser through the reversible solid-liquid transition process of the PCM. With this feature, the optimal PTT temperature of implanted PCF-based composite scaffolds was identified for tumor therapy with minimal normal tissue damage. In addition, controlled release of chemotherapeutic drugs and heat shock protein (HSP) inhibitors from the PCF-based composite scaffolds have been shown to improve the efficacy of mild PTT. The developed PCF-based scaffold sheds light on the development of a new generation of therapeutic scaffolds for thermal therapy.

Keywords

Phase change fiber; Temperature regulation; Controlled drug release; Heat shock protein; Mild photothermal-chemo therapy

TOC figure:



*Corresponding authors. E-mail address: lingewang@scut.edu.cn (Linge Wang), yujianqian@scut.edu.cn (Qianqian Yu).

1. Introduction

Cancer has become a major public health issue due to its high morbidity and mortality rates. Significant progress has been made in cancer treatment over the last few decades [1]. Among the existing treatment methods, photothermal therapy (PTT) has become a popular treatment because of its minimal biological invasiveness, high convenience, lack of systemic side effects and obvious therapeutic effect [2, 3, 4, 5]. However, precisely regulating the temperature at the tumor site in the body is difficult with traditional PTT. In most cases, the PTT temperature is higher than the appropriate temperature for completely eliminating tumor cells. Such high temperatures cause damage to normal tissue near the lesion, limiting treatment accuracy and increasing side effects [6]. This severely restricts the clinical application of PTT in cancer treatment, particularly around vital organs [7]. Therefore, one of the key issues in achieving the most effective photothermal treatment is the determination of the photothermal temperature *in situ* to completely eliminate the tumor without causing heat damage to the surrounding normal tissue [8, 9, 10].

Phase change materials (PCMs) make use of latent heat, which can be stored or released from a material over a narrow temperature range [11, 12]. PCMs absorb energy during the heating process as a phase change occurs and release energy to the environment during the reverse cooling process. The use of a latent heat storage system based on PCMs is an efficient method of storing thermal energy because of the high latent heat and isothermal nature of the storage process, which also provide the

possibility to prevent the rapid rise or fall of the PTT temperature [13]. Thus, a PCM-based therapeutic system with suitable phase transition temperature, high latent heat and shape stability is an ideal technology to regulate the local temperature of a tumor site [14]. Given that the local temperature of PTT should be kept between 42°C and 48°C, only a few PCMs with suitable phase change temperature and biosafety can be used *in vivo*. Fatty acid lauric acid (LA), with a melting point of 44°C, has been used as a solid-liquid PCM for temperature-controlled release of biomacromolecules, providing a good alternative treatment [15, 16]. However, the inherent problem of this LA-based therapeutic system relates to the difficulty of improving the heat storage density and thermal stability. One solution is to fabricate porous hollow fibers with well-defined holes, which enable increased LA loading and enhanced thermal stability. To this end, electrospinning can be used as a straightforward, scalable and versatile structural fiber production technology [17, 18]. For example, fatty acids/alcohols have been used as thermal storage materials in the fabrication of phase change fibers (PCFs) via electrospinning [19, 20]. Furthermore, when compared to nanoparticle-based PTT systems [21, 22, 23], fiber-based PTT systems are more likely to cause normal tissue thermal damage *in vivo* due to local enrichment and a lack of flow and dispersion properties. Therefore, LA-loaded PCFs with high heat storage density and shape stability could regulate photothermal temperature to achieve mild PTT and alleviate thermal damage to normal tissues.

However, mild PTT can activate cellular anti-apoptosis and cyto-protection pathways in cancer cells, particularly the heat shock response, which enhances cell

thermo-resistance [24]. Heat shock proteins (HSPs) are ubiquitous molecular chaperones in nearly all species and provide a natural protective mechanism that can correct protein misfolding to maintain activity when exposed to harmful external stimuli like hyperthermia [25]. Heat shock protein 70 (HSP70), which is overexpressed in many cancer cells, is a crucial protein in the HSP family that provides cell thermotolerance while rendering mild PTT ineffective [26]. Therefore, decreasing or inhibiting HSP70 activity in tumor cells provides an innovative strategy to achieve effective mild PTT. In addition, mild PTT is typically used in conjunction with other treatments, such as chemo and gene-therapy [27, 28]. It has been reported that when the intratumor blood flow and oxygenation are increased during PTT, tumor cells become more susceptible to chemotherapeutic drugs [29, 30]. As a result, combined photothermal-chemotherapy has the potential to significantly improve therapeutic efficacy.

Herein, a temperature-regulated PCF-based scaffold has been developed as a functional trigger for collaborative mild photothermal-chemotherapy. The preparation of PCF-based composite scaffolds is depicted in [Fig. 1a](#). Hollow carbon fibers (HCFs) with high porosity and excellent photothermal performance have been produced by electrospinning and calcining polyacrylonitrile/zeolitic imidazolate framework-8 (PAN/ZIF-8) fibers. HCFs were soaked in a methanol solution containing LA (as the PCM) with the HSP70 inhibitor, Apoptozole (Az) [30, 31], and anti-tumor drug, doxorubicin hydrochloride (DOX) to create PCF/DOX/Az scaffolds. These scaffolds, which exhibited high heat latent and thermal stability were then implanted in the tumor

site to ablate the tumor cells and alleviate excessive heat damage. Upon near infrared (NIR) laser irradiation, the PCF/DOX/Az scaffolds exhibited optimal photothermal performance, temperature regulation capability and temperature-responsive drug release behavior (Fig. 1b). Thus, this PCF-based composite scaffold shows tremendous promise in thermal therapy for temperature regulation and controlled drug release.

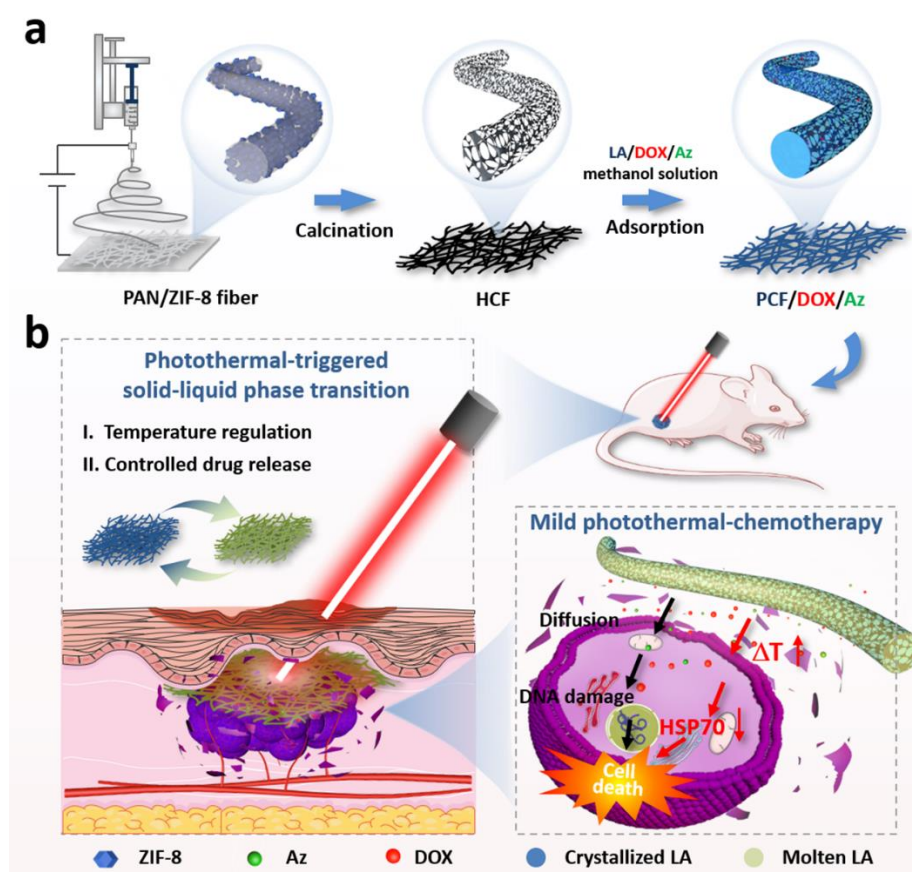


Fig. 1 Schematic diagram of the fabrication process of PCF/DOX/Az scaffolds and *in vivo* mild photothermal-chemotherapy, where **a** shows the preparation of HCFs through electrospinning and carbonization of PAN/ZIF-8 fibers, before loading LA (to produce PCFs) and bioactive molecules (to produce PCF/DOX/Az scaffolds); and **b** adjuvant mild photothermal-chemotherapy for suppressing tumor recurrence and alleviating thermal damage.

2. Experimental section

2.1 Materials

Zinc nitrate hexahydrate ($\text{Zn}(\text{NO}_3)_2 \cdot 6\text{H}_2\text{O}$), 2-methylimidazole (2-MeIM), LA and DOX were purchased from Sigma-Aldrich (Shanghai, China). PAN ($M_w = 150,000$ g/mol) was commercially obtained from Sipin Technology Co. (Hefei, China). Az was purchased from Zeye Biological Technology Co. (Shanghai, China) and *N, N*-dimethylformamide (DMF) from Guangzhou Chem. Co. (Guangzhou, China). Actin-tracker green-488, cell counting kit-8 (CCK-8), and calcein acetoxymethyl ester/propidium iodide (Calcein AM/PI) were purchased from Beyotime Biotechnology (China). Hematoxylin-Eosin (H&E), terminal-deoxynucleotidyl transferase mediated nick end labeling (TUNEL), Ki67 and heat shock protein 70 (HSP70) staining kit were purchased from Servicebio (China). Unless otherwise specified, all reagents were used as received.

2.2 Cell lines and animals

South China University of Technology (SCUT, Guangzhou, China) provided human umbilical vein vessel endothelial cells (HUVECs) and mouse mammary carcinoma cell line 4T1 cells. All of the cells were grown in a humidified incubator (5% CO_2 , 37°C). Female BALB/c mice (25 ± 2 g) were fed in SCUT's Experimental Animal Center. All animal experiments were authorized by SCUT's Institutional Animal Care and Use

Committee (AEC No. 2020048) and carried out in accordance with the Laboratory Animal Care and Use Guidelines.

2.3 Preparation of ZIF-8 and PAN/ZIF-8 fibers

The synthesis of ZIF-8 was carried out as follows: 2.26 g $\text{Zn}(\text{NO}_3)_2 \cdot 6\text{H}_2\text{O}$ and 2.64 g 2-MeIM were dissolved in 400 mL methanol. After stirring for 16 h, the product was collected and washed three times with methanol. PAN/ZIF-8 fibers were prepared via electrospinning [32]. 1 g PAN and 0.7 g ZIF-8 were added to 9 g of DMF and stirred at 60°C for 24 h. A homogeneous precursor solution was loaded into a syringe for electrospinning, with the voltage set to 16 kV. The needle-to-collector distance was fixed at 15 cm, and PAN/ZIF-8 fibers were collected on aluminum foil and dried at 30°C.

2.4 Preparation of HCF and PCF/DOX/Az composite scaffold

The as-prepared PAN/ZIF-8 fibers were transferred to a tube furnace and carbonized for 3 hours at 1,100°C in an argon atmosphere to produce HCFs. 20 mg of the HCFs were immersed in a methanol solution containing LA, Az and DOX for 12 hours to produce the PCF/DOX/Az composite scaffold.

2.3 Material characterization

The morphologies of the ZIF-8, PAN fibers, PAN/ZIF-8 fibers, HCFs and PCF/DOX/Az scaffolds were observed by scanning electron microscopy (SEM) and

transmission electron microscopy (TEM). X-ray diffraction (XRD), nitrogen adsorption/desorption isotherms and X-ray photoelectron spectroscopy (XPS) were used to analyze the structure and components of as-prepared fibers. Differential scanning calorimetry (DSC) and thermogravimetric analysis (TGA) were used to examine the thermal performance and LA content of PCF/DOX/Az scaffolds, respectively. To further validate the phase change behavior of the PCF-based composite scaffolds (by identifying the melting and crystallizing behavior), *in situ* time-resolved wide angle X-ray diffraction (WAXD) was performed during heating from 37 to 49°C and then cooling from 49 to 37°C at a rate of 3°C/min.

2.5 Photothermal and energy storage performance of PCF/DOX/Az scaffold

To verify the thermal energy storage performance of the PCF-based composite scaffolds, 20 mg of PCF/DOX/Az scaffolds were placed on a heating platform and heated at a rate of 3°C/min from 37°C for 10 minutes before cooling naturally for 10 minutes. The temperature of the scaffold was measured during the heating and cooling ramps. The photothermal and energy storage properties of HCFs and PCF/DOX/Az scaffolds were also investigated after 10 minutes of NIR laser irradiation. Temperature variations were recorded at 30 second intervals.

2.6 *In vitro* drug release

The DOX release profiles of PCF/DOX/Az scaffolds were evaluated with and without laser irradiation. 20 mg of PCF/DOX/Az scaffolds were soaked in 5 mL phosphate

buffer solution (PBS). At the predetermined time interval, 1 mL of the PBS was withdrawn and an equivalent volume of fresh PBS was added. The amount of released DOX was recorded by Spectra Max iD3 and calculated by the standard DOX curve. The accumulative released DOX was calculated using the following equation (1):

$$\text{Accumulative release (\%)} = \frac{w_{\text{released DOX}}}{w_{\text{total DOX}}} \times 100\% \quad (1)$$

where $w_{\text{released DOX}}$ is the accumulative weight of released DOX from the PCF/DOX/Az scaffold and $w_{\text{total DOX}}$ is the total weight of DOX in the pristine PCF/DOX/Az scaffold.

2.7 *In vitro* biocompatibility assay

To assess the biocompatibility of the various scaffolds, HUVECs were cultured in DMEM supplemented with 10% fetal bovine serum (FBS), 100 IU/mL of penicillin, and 100 $\mu\text{g/mL}$ of streptomycin. Sterilized PCFs, HCFs, PCF/DOX and PCF/DOX/Az scaffolds were placed in 24-well plates. HUVECs with 2.0×10^4 cells/well were then seeded and incubated for 1 day and 3 days in a humidified cell incubator (5% CO_2 , 37 $^\circ\text{C}$). HUVECs were also cultured in blank wells as a control (Ctrl). Calcein-AM/PI was used for Live/Dead staining and CCK-8 assay was performed to quantitatively assess the cell viability.

2.8 *In vitro* antitumor efficacy

The 4T1 cells were cultured in DMEM supplemented with 10% FBS, 100 IU/mL of penicillin, and 100 $\mu\text{g/mL}$ of streptomycin. 4T1 cells with 2.0×10^4 cells/well were

seeded in 24-well plates and cultured in an incubator (37°C, 5% CO₂). Sterilized PCFs, HCFs, PCF/DOX and PCF/DOX/Az scaffolds were placed in 24-well plates. NIR laser irradiation with 0.5 W/cm² was turned on for 10 minutes (3 times). Calcein-AM/PI was used for Live/Dead staining and the cell viability was determined by CCK-8 assay with and without laser irradiation. To assess HSP70 expression in tumor cells before and after laser irradiation (5 min), tumor cells from different groups were incubated in the dark at 4°C overnight with Anti-HSP70 Rabbit mAb, followed by incubation with FBS and Cy3 conjugated Goat Anti-rabbit IgG (H + L) for 1 h. Tumor cells were also stained with Phalloidin-Fluorescein isothiocyanate (FITC) and DAPI before being rinsed with PBS and observed using confocal laser scanning microscopy (CLSM). *In vitro* wound healing and Transwell experiments were performed to assess the inhibitory effect of laser-treated scaffolds on migration and invasion ability. In the wound healing tests, confluent tumor cell cultures were wounded with a 200 µL micropipette tip and immediately placed in a serum-free medium supplemented with Ctrl, PCFs, PCF/DOX/Az scaffolds, and PCF/DOX/Az scaffolds + Laser treatment (3 × 10 minutes). Bright-field images of damaged tumor cell monolayers with various treatments were acquired at 0, 12, 24, and 36 h. ImageJ software was used to determine the extent of wound closure after three wound measurements were obtained. The Transwell experimental procedure was as follows: a serum-free suspension of hungry tumor cells was inoculated in the Transwell chamber for co-culture with the prepared scaffolds, and a 20% fetal bovine serum medium was added to the lower chamber. After laser irradiation and bubble removal, the chamber was placed in an orifice plate for 24

hours of culture. ImageJ software was used to count the tumor cells that had invaded the lower ventricle.

2.9 *In vivo* antitumor efficacy

Tumor-bearing mice were modeled similarly to the previous work [4]. Mice were randomized into 7 groups (n = 6): (G1) Ctrl, (G2) PCFs, (G3) PCF/DOX, (G4) PCF + Laser, (G5) PCF/DOX scaffolds + Laser, (G6) PCF/DOX/Az scaffolds + Laser, and (G7) HCFs + Laser. For laser treating groups, each mouse was treated with laser irradiation of 0.5 W/cm² for 10 minutes at day 1, 3, 5, and 7. Temperature changes and thermal images of the tumor site were monitored using an infrared thermal camera. Every 3 days, the dimensions of the recurrent tumors were measured.

2.10 Statistical analysis

All experiments were carried out in triplicate or more, and all quantitative results are expressed as an average with mean \pm standard deviation (SD). One-way Analysis of Variance (ANOVA) was used to determine the statistical significance differences. P values of * < 0.05, ** < 0.01, and *** < 0.001 were considered significant for the differences.

3. Results and Discussion

3.1 Preparation and characterization of PCF/DOX/Az scaffolds

Firstly, a PAN/ZIF-8 solution was electrospun into a fiber precursor (Fig. S1a). Hexahedral ZIF-8 nanoparticles with an average size of approximately 50 nm and a smooth surface were successfully pre-synthesized as shown in Fig. S1b-d. The preparation process of HCFs and PCFs is depicted in Fig. 2a. From the SEM and TEM images, the prepared PAN/ZIF-8 fibers had a cylindrical shape, and the ZIF-8 nanoparticles were well-dispersed in the PAN fibers (Fig. 2b, c). When compared to pure PAN fibers (Fig. S1e-g), the surface of PAN/ZIF-8 fibers was very rough, owing to the high ZIF-8 content (70 wt%) and the fiber diameter increased from 255 ± 47 nm to 289 ± 58 nm (Fig. 2d). After carbonizing PAN/ZIF-8 fibers at 1,100°C in an argon atmosphere, HCFs were obtained [33]. A color change was observed from white PAN/ZIF-8 fibers to black HCFs, accompanied by a significant size shrinkage to an average diameter of 195 ± 37 nm, as observed by digital camera, SEM and TEM, confirming success of the carbonization process (Fig. 2e-g). PCFs were prepared by immersing HCFs in a methanolic solution of LA. The effect of initial LA concentration on the content of LA in the PCFs was investigated. TEM images in Fig. S2a-c show that the porous structure within the HCFs filled to varying degrees after LA adsorption. TGA was used to determine the LA loading within the HCFs. PCFs degraded at temperatures ranging from 100°C to 250°C, as shown in Fig. S2d, which is attributed to LA decomposition. The content of LA within the PCFs increased from 78.9% to 86.1%

and then decreased to 82.7% as LA concentration increased from 250, 500, to 750 mg/mL. The solid-liquid phase transition in PCF is required to control the photothermal energy storage and release and drug release behavior more effectively, as such, the LA concentration was fixed at 500 mg/mL in the remaining studies to maximize the phase change performance. PCF/DOX/Az scaffolds were then prepared by immersing HCFs in a methanolic solution containing LA (500 mg/mL), DOX (2 wt%), and Az (20 μ M).

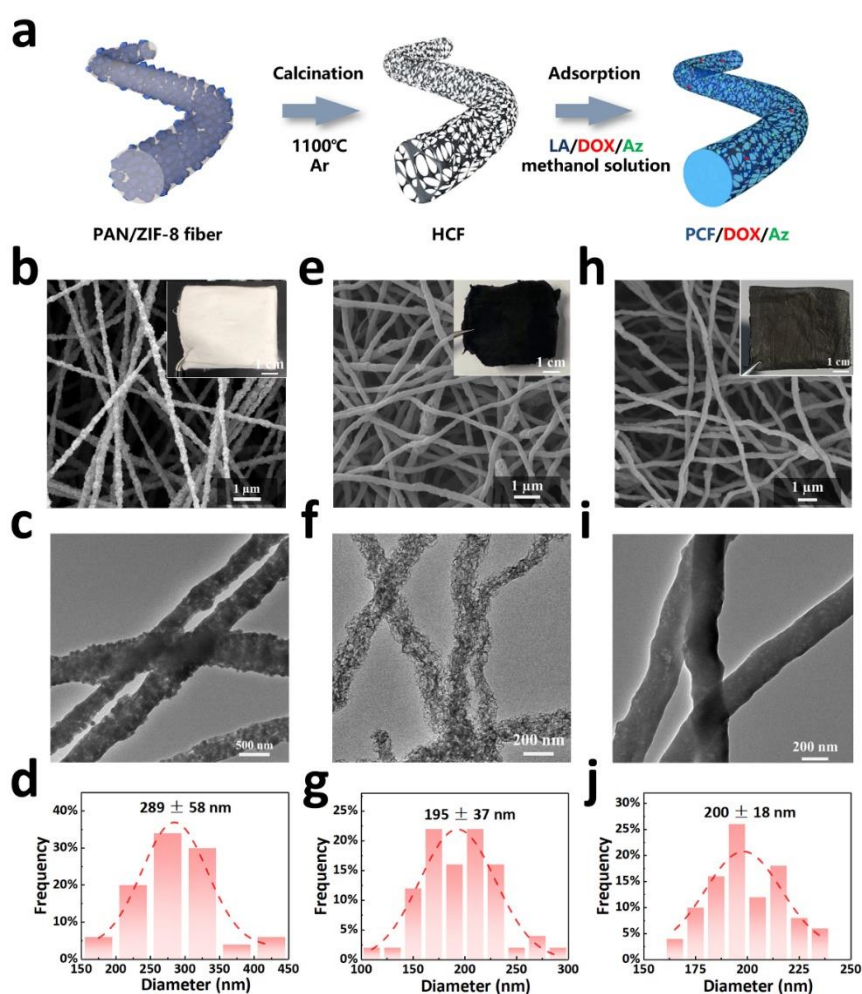


Fig. 2 Morphology of prepared fibers. **a** Fabrication process of PCF/DOX/Az scaffolds; **b, c, d** SEM images (inserted with optical photograph), TEM images and size distribution of PAN/ZIF-8 fibers; **e, f, g** SEM images (with optical photograph inserts), TEM images and size distribution of HCFs; **h, i, j** SEM images (with optical photograph inserts), TEM images and size distribution of PCF/DOX/Az scaffolds.

XRD was used to determine the phase purity of the pristine ZIF-8 nanoparticles and the ZIF-8 nanoparticles within the PAN/ZIF-8 fibers. Fig. 3a shows the diffraction patterns of pristine ZIF-8 nanoparticles, PAN fibers and PAN/ZIF-8 fibers. The ZIF-8 nanoparticles show peaks at 7.3° , 10.3° , 12.7° , 14.7° , 16.4° , and 18.0° , and the PAN fibers show a single peak at 16.8° . The PAN/ZIF-8 fibers show peaks at 7.3° , 10.3° , 12.7° , 14.7° , 16.4° , 16.8° and 18.0° , demonstrating that the pre-synthesized ZIF-8 was in its pure phase and was stable within the PAN fibers [34]. HCFs show two broad peaks at $2\theta = 26.5^\circ$ and 42.5° in the XRD pattern, which correspond to the (002) and (100) crystal planes of graphite, respectively (Fig. 3b). Well-defined pore structures within HCFs were formed by the decomposition of ZIF-8 nanoparticles and the evaporation of Zn (melting point 420°C , boiling point 907°C) at $1,100^\circ\text{C}$. From the XRD patterns, the strong diffraction peaks of pristine LA at $2\theta = 19.2^\circ$, 19.9° , 21.7° , 23.5° , 24.5° , and 26° were observed in PCF/DOX/Az scaffolds, indicating the successful encapsulation of LA, DOX and Az. From the nitrogen adsorption-desorption isotherms and pore size distributions of PAN/ZIF-8 fibers and HCFs depicted in Fig. 3c-d, type IV isotherms with hysteresis loops were observed. Due to the strong interaction between the adsorbent and porous fiber surface, the adsorption capacity rapidly increased in the low P/P_0 regime. The isotherms were convex and the adsorption increased gradually in the middle P/P_0 range due to capillary condensation. The specific surface area of the PAN/ZIF-8 fibers was $414.58\text{ m}^2/\text{g}$, with average pore diameter of 4.7 nm , whereas the HCFs displayed a specific surface area of $1187.86\text{ m}^2/\text{g}$ and

average pore diameter of 4.6 nm. Notably, the specific surface area of calcined fibers increased significantly, laying the groundwork for PCMs with high loading.

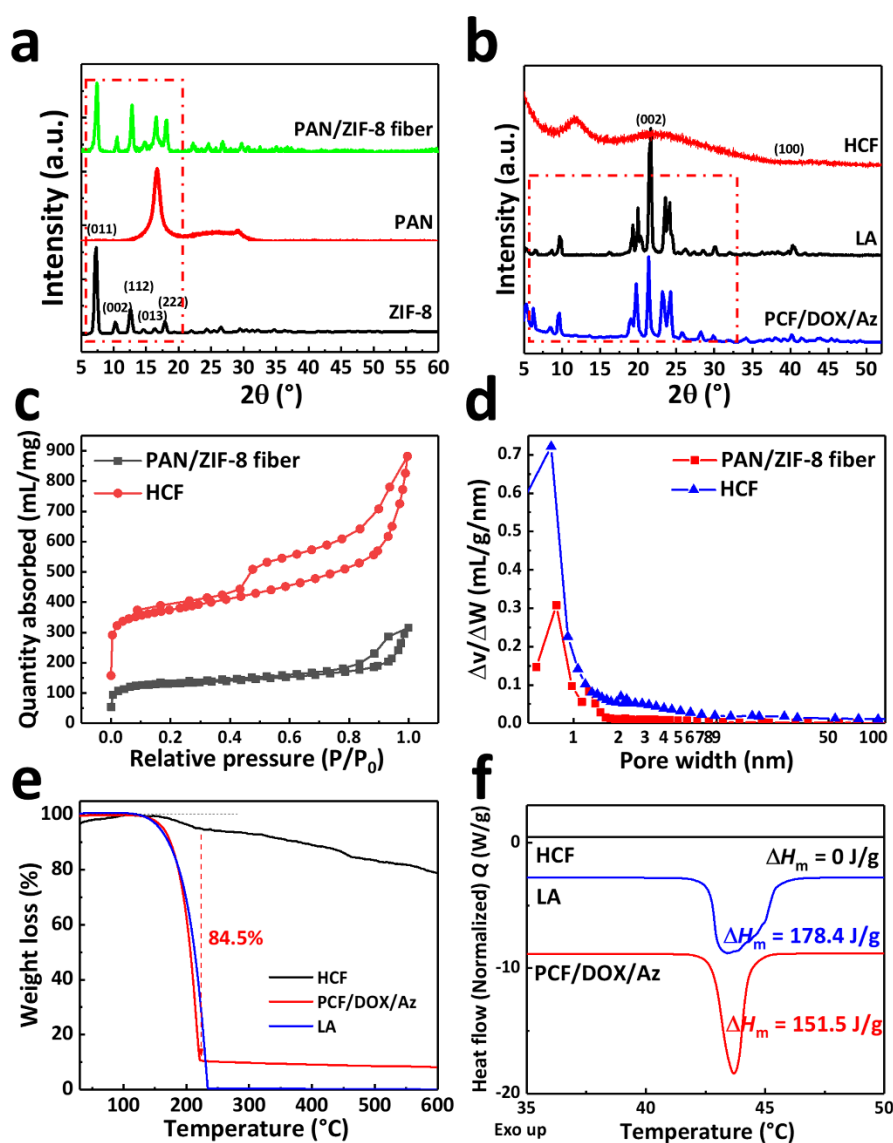


Fig. 3 a XRD patterns of ZIF-8, PAN and PAN/ZIF-8 fibers; b XRD patterns of HCFs, LA and PCF/DOX/Az scaffolds; c-d nitrogen adsorption-desorption isotherms and pore width of PAN/ZIF-8 fibers and HCFs; e TGA thermograms of HCFs, LA and PCF/DOX/Az scaffolds; f DSC thermograms of HCFs, LA and PCF/DOX/Az scaffolds.

HCFs were further characterized by XPS. As shown in Fig. S3a-b, the existence of C1s, N1s and O1s in the HCFs was observed and the N1s spectrum can be further

resolved into four different peaks at 398.4 eV, 400.1 eV, 401.2 eV, and 403 eV, which are assigned to pyridinic-N, pyrrolic-N, graphitic-N, and oxidized-N, respectively. TGA thermograms show that HCFs had only a minor amount of thermal decomposition, whereas LA showed complete thermal decomposition. PCF/DOX/Az scaffolds also demonstrated thermogravimetric phenomena in this temperature range (Fig. 3e). DSC thermograms also show that HCFs had no obvious melting process in the temperature range of 35 - 55°C, whereas LA and PCF/DOX/Az scaffolds both have melting peaks at around 43.4°C, with latent heat of 178.4 J/g and 151.5 J/g, respectively (Fig. 3f).

3.2 Thermal energy storage and photothermal conversion of PCF/DOX/Az scaffolds

Continuous heating and cooling treatments were used to fully probe the phase change behavior of LA and the thermal stability of the PCFs. The DSC thermograms of a representative PCF sample during 25 continuous heating-cooling cycles are shown in Fig 4a. The T_m and crystallization temperature (T_c) of LA within PCFs were consistently around 43.4°C and 39.2°C, respectively, during the heating-cooling cycles. In addition, the ΔH_m and enthalpy of crystallization (ΔH_c) were consistently around 153.7 J/g and 152.8 J/g, respectively, over 25 cycles. The high thermal stability of PCFs is attributed to the encapsulation effect of LA in the nanochannels (as observed in the TEM images), and demonstrates that there was no obvious leakage of LA from HCFs (Fig. 4b). Furthermore, time-resolved *in situ* wide angle X-ray diffraction (WAXD) was used to confirm the solid-liquid phase transition of LA within the PCFs [35]. In the WAXD

experiment, the temperature was increased from 37°C to 49°C at 3°C/min, kept isothermal for 5 minutes, and then decreased from 49°C to 37°C at 3°C/min, which is in line with the temperature profile of clinical PTT. The integrated WAXD profiles depicted the phase-change behavior of PCFs during one heating and cooling cycle (Fig. 4c-d). Crystallization peaks of LA ($2\theta = 21.7^\circ$ and 23.5°) were observed in the temperature range of 37 - 48°C, indicating the high crystallinity of LA within the PCFs. When the temperature rises above 40°C, the characteristic peaks of LA diminish, indicating that the solid-liquid phase transition of LA has occurred within PCF. After being isothermal for 5 minutes, the cooling procedure was carried out. The crystallization peak of LA appeared and grew stronger as the temperature dropped below 40°C.

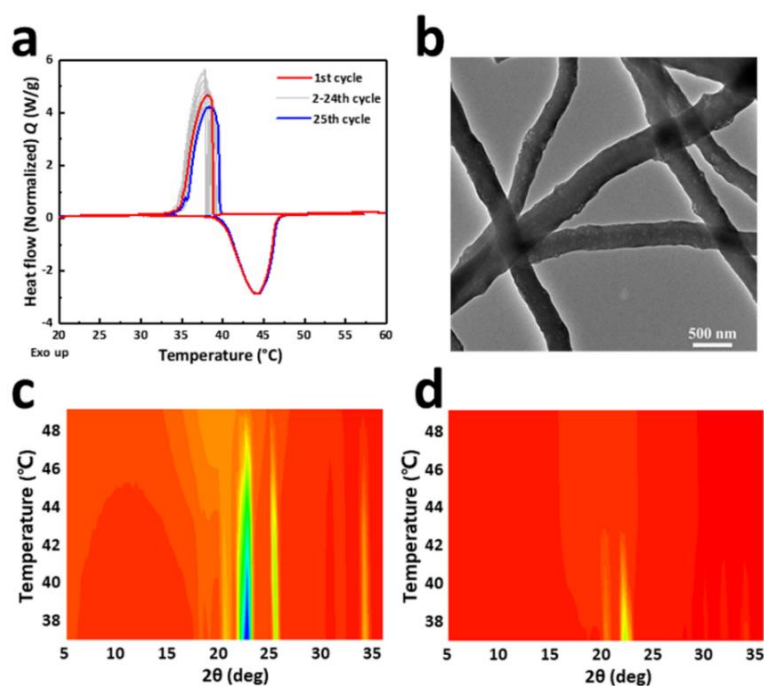


Fig. 4 Thermal performance of PCF/DOX/Az scaffolds. **a** DSC thermograms of PCF/DOX/Az scaffolds during 25 continuous heating-cooling cycles; **b** TEM images

of PCF/DOX/Az scaffolds after 25 heating-cooling cycles; **c-d** time-resolved *in situ* WAXD data of thermal-responsive PCF scaffold.

The temperature change of HCFs and PCF/DOX/Az scaffolds under heating and cooling conditions was further investigated as shown in **Fig. 5a**. The temperature of HCFs and PCF/DOX/Az scaffolds gradually increased from 37°C during the heating process. After heating for 10 minutes, the temperature of the HCFs increased linearly to 61.5°C, whereas the PCF/DOX/Az scaffolds displayed a clear plateau at 42.7°C, which lasted approximately 2 minutes. The temperature of PCF/DOX/Az scaffolds continued to rise after the plateau, reaching 58.7°C after 10 minutes of heating. During the 10 minute cooling process, the temperature of the HCFs dropped linearly to 37°C. In contrast, when the temperature of the PCF/DOX/Az scaffolds was reduced to 43.4°C, a clear plateau appeared that lasted approximately 2 minutes. The temperature of PCF/DOX/Az scaffolds continued to decrease after the plateau, reaching approximately 37°C. The melting and crystallization temperatures of LA match the plateauing temperature of the PCF/DOX/Az scaffolds during heating and cooling, indicating that plateauing occurs due to the endothermic melting and exothermic crystallization behavior of LA [36].

To characterize the *in vitro* photothermal property and thermal energy storage performance, HCFs and PCF/DOX/Az scaffolds were irradiated by NIR laser and the real-time temperature changes were monitored. **Fig. 5b** depicts the temperature variation of LA and HCFs after 10 minutes of NIR laser irradiation at various power densities. The temperature of HCFs increased to 52.4°C, 74.5°C, and 118.2°C, with an

increase in power density ($0.5 \text{ W}\cdot\text{cm}^{-2}$, $0.75 \text{ W}\cdot\text{cm}^{-2}$, and $1 \text{ W}\cdot\text{cm}^{-2}$, respectively), indicating that laser power density has a significant influence on the temperature of the HCFs. In the heating-cooling treatment of HCFs, however, no temperature plateau was observed. It is impossible to achieve the thermal energy storage and release by simple HCFs, without an incorporated PCM. Following laser irradiation at $0.5 \text{ W}\cdot\text{cm}^{-2}$, $0.75 \text{ W}\cdot\text{cm}^{-2}$ and $1 \text{ W}\cdot\text{cm}^{-2}$, the temperature of PCF/DOX/Az scaffolds rapidly rose from room temperature to $\sim 43^\circ\text{C}$, followed by a clear plateau. During the cooling process, the temperature of PCF/DOX/Az scaffolds decreased gradually and another temperature plateau was observed in the range of $44 - 41^\circ\text{C}$ (Fig. 5c and Fig. S4). In addition, the laser power density was fixed at $0.5 \text{ W}\cdot\text{cm}^{-2}$ in subsequent experiments to prevent excessive heat from exceeding the absorption of PCFs. The two temperature plateaus of PCF/DOX/Az scaffolds in the heating-cooling cycle can be attributed to the storage of photothermal energy and the release of latent heat as a result of the phase-change behavior of encapsulated LA. This indicates that the photothermal conversion capability of PCF/DOX/Az scaffolds, and its maximum temperature reached, are significantly lower than those of HCFs under laser irradiation ($0.5 \text{ W}\cdot\text{cm}^{-2}$). The light-to-thermal energy conversion and storage efficiency η of PCF/DOX/Az scaffolds can be calculated by the following equation (2) [37]:

$$\eta = \frac{m\Delta H}{\rho S(t_f - t_i)} \quad (2)$$

Where m is the mass of the sample (0.1 g), ΔH is the enthalpy obtained by DSC (151.5 J/g), ρ is the intensity of laser irradiation ($0.5 \text{ W}\cdot\text{cm}^{-2}$), S is the surface area of sample (0.36 cm^2), and t_i and t_f are the starting and terminating time before and after

the phase transition (120 s), respectively. The calculated η of PCF/DOX/Az scaffolds was 70.1%, indicating that LA loaded within the scaffolds exhibits good thermally responsive solid-liquid phase transformation ability and can be used for long-term heat energy storage and release.

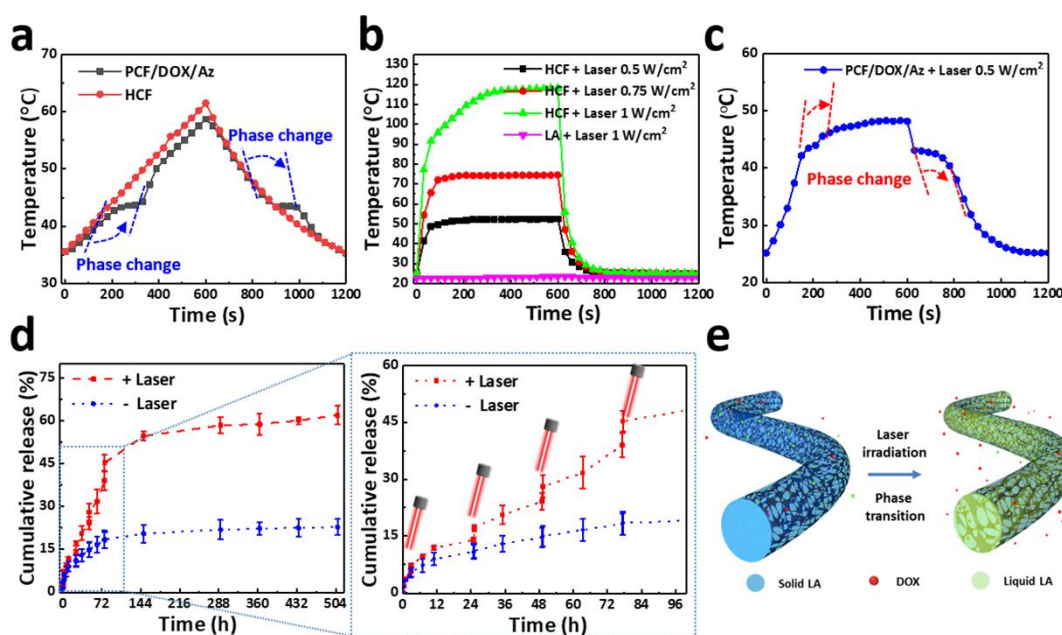


Fig. 5 Photothermal performance and drug release behavior of PCF/DOX/Az scaffolds. **a** Heating-cooling curves of HCFs and PCF/DOX/Az scaffolds; **b** Temperature profiles of NIR laser treated LA and HCFs with different laser power density; **c** Temperature profile of laser treated ($0.5 \text{ W}\cdot\text{cm}^{-2}$) PCF/DOX/Az scaffolds; **d** Laser-triggered release of DOX from PCF/DOX/Az scaffolds; and **e** schematic of the thermally triggered drug release behavior of PCF/DOX/Az scaffolds. The data are shown as mean \pm SD ($n = 3$).

3.3 *In vitro* drug release

The solid-to-liquid phase transition of LA is known as a significant factor for controlling drug release [38, 39]. Therefore, the temperature-responsive cumulative release profiles of DOX from PCF/DOX/Az scaffolds were investigated with and

without laser irradiation as illustrated in Fig. 5d. Without laser irradiation, only around $5.68 \pm 0.57\%$ of DOX was released in 160 minutes, whereas approximately $7.25 \pm 0.45\%$ of DOX was released with laser irradiation (10 min). After four laser irradiations over a 21-day period, the amount of DOX released in the PCF/DOX/Az scaffolds was $61.94 \pm 3.33\%$, whereas the amount of DOX released from the PCF/DOX/Az scaffold without laser irradiation was only $22.73 \pm 2.84\%$. Thus, it can be concluded that drug release was primarily from the surface of the PCF-based composite scaffold during the first 72 hours, with limited drug release occurring during the remainder of the time due to the crystallization zone preventing drug diffusion into the aqueous environment without laser irradiation. There was clear burst release behavior observed with laser irradiation, as shown in Fig. 5e, which is attributed to the phase change of LA caused by the laser-induced temperature variation. In summary, the prepared PCF scaffolds can be used as a photothermal-responsive gatekeeper to control the release of anticancer drug and other active biomolecules.

3.4 *In vitro* biocompatibility

The biocompatibility of the prepared scaffolds was assessed prior to *in vitro* and *in vivo* antitumor experiments. For 1 and 3 days, HUVECs were seeded in 96-well plates with PCFs, PCF/DOX, PCF/DOX/Az scaffolds, HCFs and no scaffold as a control (Ctrl). There was no clear observation of PI-stained HUVECs in the fluorescence images shown in Fig. S5a, indicating that the prepared scaffolds were not toxic to normal cells. The CCK-8 assay was used to quantify cell viability and proliferation (Fig.

S5b-c). The results showed that HUVECs had a high survival rate and clear cell proliferation. The viability of HUVECs remained above 85% when cultured with different scaffolds, indicating that these scaffolds exhibit biocompatible behavior.

3.5 *In vitro* antitumor effect

The antitumor effect of these prepared scaffolds was investigated *in vitro* after confirming their biocompatibility. Ctrl, PCFs, PCF/DOX, PCF/DOX/Az scaffolds, and HCFs were used to treat 4T1 cells with and without laser treatment. The cell viability of treated 4T1 cells was determined using the Live/Dead staining method and the CCK-8 assay. The apoptosis of cells without laser irradiation was studied first. CLSM images of Live/Dead staining in Fig. 6a show that living cells (labelled green) were observed in Ctrl, PCF, and HCF groups, whereas a few dead cells (labelled red) were observed in PCF/DOX and PCF/DOX/Az groups. CCK-8 assays in Fig. 6b show that the cell viability of Ctrl, HCF, PCF, PCF/DOX and PCF/DOX/Az groups without laser irradiation were ~103.9%, ~101.5%, ~73.1%, ~66.3%, and ~104.6%, respectively, indicating that a single scaffold or antitumor drug has insufficient ability to kill all tumor cells. After laser irradiation, no dead cells were observed in the Ctrl group, whereas different numbers of dead cells appeared in other groups. Compared with PCF/DOX, PCF/DOX/Az showed higher cell killing efficiency. The cell viability of Ctrl, PCF, PCF/DOX, PCF/DOX/Az and HCF groups with laser irradiation were ~97.4%, ~69.2%, ~42.0% and ~2.4% respectively, which proved that the synergistic effect of mild photothermal and chemotherapy could successfully kill tumor cells. The

synergistic index was evaluated using the mortality rate of the 4T1 cells (30.8% for PCF + Laser, 58.0% for PCF/DOX, and 97.6% for PCF/DOX/Az + Laser) and analyzed using Jin's formula [40]. The synergistic index was 1.38, indicating a synergistic effect (index > 1.15) of mild photothermal and chemotherapy treatment. In addition, only a few 4T1 cells survived in the Live/Dead staining images of the HCF group and the cell viability was ~41.6%. The results clearly demonstrate the excellent antitumor efficiency of excessive heat *in vitro*, but it could also cause damage any surrounding normal cells.

[Fig. S6](#) depicts HSP70 immunofluorescence images and statistical analysis of the average fluorescence intensity of tumor cells co-cultured with various scaffolds without and with laser irradiation. HSP70 expression in tumor cells co-cultured with different scaffolds was low without laser irradiation, and the cell shape was normal with obvious skeleton spreading. Except for the PCF/DOX/Az group, the expression level of HSP70 was higher in the other groups after laser irradiation, particularly in the HCF group, which was primarily due to the temperature of HCFs being higher than other groups due to the absence of temperature regulation function. The lower expression of HSP70 in the PCF/DOX/Az group was due to an inhibition effect caused by the release of HSP70 inhibitor, Az, from the scaffolds after laser irradiation. Except for the Ctrl group, the tumor cell morphologies of the other groups changed significantly after laser irradiation, and the cell structure changed from being spread to becoming more rounded, primarily due to photothermal damage to tumor cells.

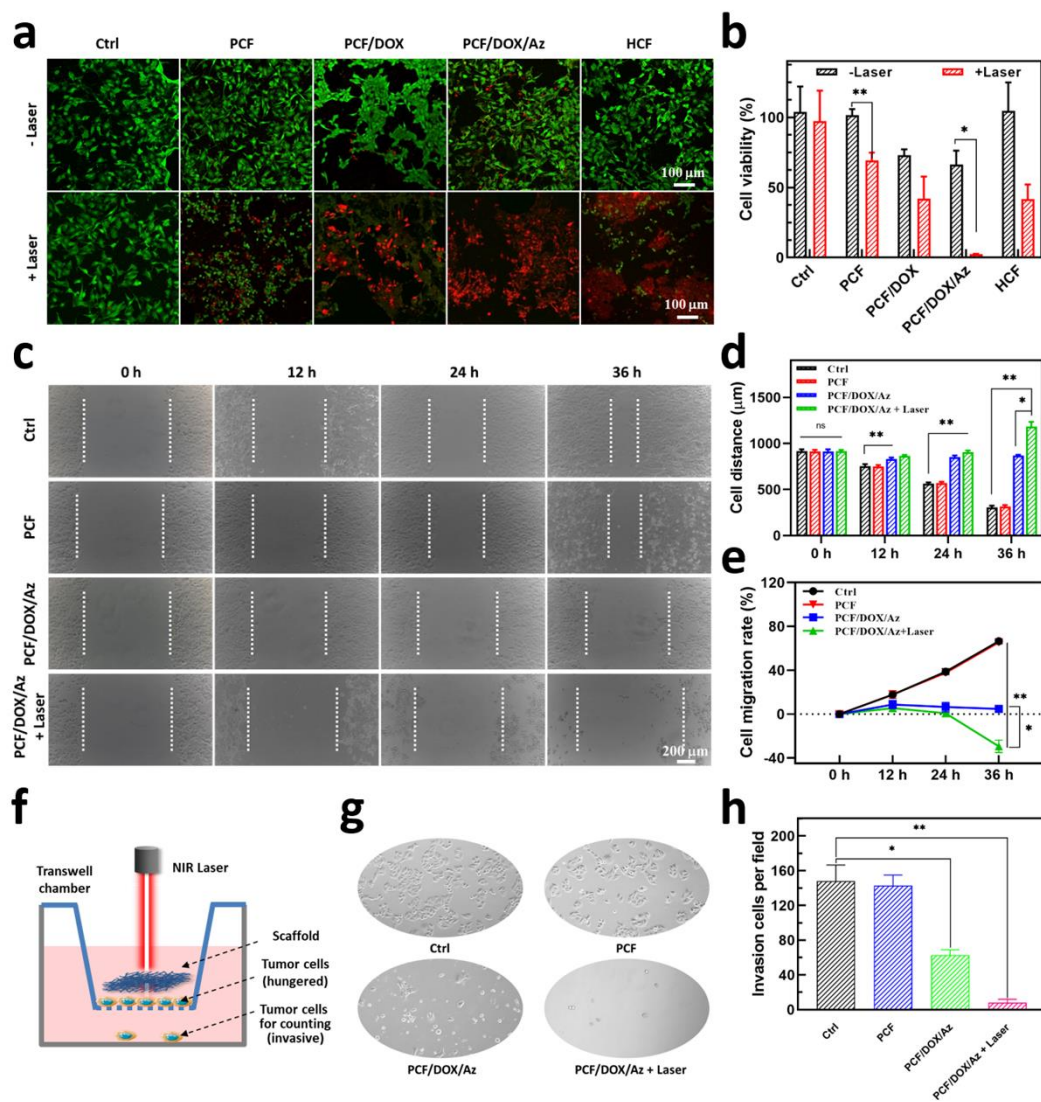


Fig. 6 *In vitro* anti-tumor effect of PCF-based composite scaffolds. **a** Live/Dead staining images of tumor cells following treatment with different groups; **b** Cell viability of tumor cells following treatment with different groups; **c** Cell migration observed by optical microscopy after different treatments; **d** Statistical analyses of the average spacing of cell patterns; **e** Cell migration rates of tumor cells after different treatments; **f** Schematic diagram of the Transwell experiment; **g** Invasive tumor cells observed by optical microscopy after different treatments; **h** Statistical analyses of the numbers of invasive tumor cells. The data are shown as mean \pm SD ($n = 3$), $P < 0.05$ (*), $P < 0.01$ (**) and $P < 0.001$ (***)

Additionally, local migration and invasion of tumor cells to the surrounding extracellular matrix (ECM) is a major cause of tumor recurrence and metastasis. The anti-migration and anti-invasion properties of the various PCF-based composite scaffolds were further studied *in vitro*. A wound healing test was performed to observe the inhibition of tumor cell migration by PCF-based scaffolds [41]. As shown in Fig. 6c-e, tumor cells in the Ctrl group gradually migrated in the interstitial space of the wound over time, reaching 66.5% of the wound spacing after 36 hours of culture, whereas tumor cells in the PCF/DOX/Az, and PCF/DOX/Az + Laser groups rarely entered the interstitial space of the wound. At 36 hours, cell migration rates reached 4.8%, and -29.4%, respectively. Tumor cells treated with PCF/DOX/Az + Laser failed to grow into the wound area, and cell density decreased dramatically as a result of photothermal-chemo-induced cell apoptosis, indicating an inhibitory effect on tumor cell migration. Fig. 6f depicts a schematic diagram of the Transwell experiment, optical microscopy images of invading tumor cells in the lower chamber, and a statistical analysis of the number of invading cells [42]. In comparison to the Ctrl group (approximately 148 cells/field), the number of invasive tumor cells in the PCF group was not significantly reduced (about 143 cells/field), whereas the number of invasive tumor cells in the PCF/DOX/Az and PCF/DOX/Az + Laser groups was significantly reduced. The number of invasive tumor cells in the PCF/DOX/Az + Laser group was only 8 cells/field, and the cell structure was clearly damaged, indicating that the inhibitory effect of PCF/DOX/Az + Laser on tumor cell invasion was significantly better than that of the other groups (Fig. 6g-h).

3.6 *In vivo* photothermal imaging and FL/MR imaging

The anti-tumor recurrence and metastasis inhibition of PCF-based composite scaffolds were tested *in vivo* [43]. 4T1 tumor cells-bearing female BALB/c mice were successfully established as a model. The mice were randomized into 7 groups (n = 6): (G1) Ctrl, tumor-bearing mice implanted with no scaffold; (G2) PCFs; (G3) PCF/DOX; (G4) PCFs + Laser; (G5) PCF/DOX + Laser; (G6) PCF/DOX/Az + Laser; and (G7) HCFs + Laser. The surgical tumor reduction and *in vivo* imaging treatment schedule are given in Fig. S7a. To confirm the *in vivo* photothermal effect of PCF-based composite scaffolds, an infrared thermal camera was used to track temperature changes in 4T1 tumor-bearing mice of G1, G6 and G7. As shown in Fig. S7b-c, after 10 minutes of laser irradiation, the temperature of the surgical lesion in G1 was not significantly elevated, indicating that laser irradiation alone could not generate adequate heat *in vivo* without the assistance of photothermal conversion materials [44]. In contrast, as the irradiation time was increased, the tumor site temperature in G6 and G7 increased to around 47.3°C and 51.7°C, respectively. These findings suggest that PCF/DOX/Az scaffolds and HCFs implanted in animals can absorb NIR laser and undergo photothermal transformation *in vivo*. The temperature of the implanted PCF/DOX/Az scaffolds was slightly lower than that of the HCFs, which is attributed to the endothermic melting effect of LA and the low thermal conductivity of PCF-based composite scaffolds.

The feasibility of monitoring the implanted PCF/DOX/Az scaffolds and remotely guiding PTT was assessed using *in vivo* fluorescence/magnetic resonance imaging (FL/MR) [45, 46]. The fluorescence signals were detected at four time points (days 1, 7, 14, and 21) using an *in vivo* FL imaging system, taking advantage of the strong inherent red fluorescence of DOX. As shown in Fig. S7d-e, the fluorescence intensity of G6 decreased with time and was distributed around the tumor site following periodic laser irradiation, indicating the laser-triggered release of DOX, whereas no fluorescence signal of G1 was observed. As shown in Fig. S7f, T2-weighted MR imaging at the four time points (1, 7, 14, and 21 days) revealed the different tumor recurrence at the cross-section of the surgical lesion of G1 and G6. During treatment, no significant solid tumors were found in G6, whereas solid tumors in G1 grew over time and became almost life-threatening. *In vivo* FL and MR imaging can help make a comprehensive diagnosis of tumor recurrence during postoperative treatment by describing the state of the implanted PCF-based composite scaffolds.

3.7 *In vivo* antitumor efficacy

Based on the high anticancer effect *in vitro*, the inhibitory effect of PCF-based composite scaffolds was further confirmed *in vivo*. Fig. 7a depicts the surgical and implantation process including anesthetization, tumor exposure, tumor removal, scaffold implantation, and suture. Tumor volume changes in mice from different groups were measured using digital calipers every three days for three weeks. On day 21, the average recurring tumor volume was approximately (G1) 1813.0 mm³, (G2) 1731.2

mm³, and (G3) 1285.4 mm³, indicating that post-operative tumor recurrence is evident in the absence of effective treatment. However, the average recurring tumor size was approximately (G4) 613.7 mm³, (G5) 119.9 mm³, (G6) 2.2 mm³ and (G7) 459.1 mm³. Notably, when tumor-bearing mice were treated with PCF/DOX/Az + Laser, tumor weight was reduced by 92.7% at day 21 and the corresponding tumor photographs are shown in [Fig. 7b-d](#). Due to the high temperature, the therapeutic effect of G7 is greater than that of G4, but due to the restriction of single PTT, the treatment effect of G7 is smaller than that of G6, and the skin tissue damage produced by G7 is greater. Furthermore, the body weight of the mice in different groups gradually increased over 21 days, with no significant difference evident between groups in [Fig. 7e](#), demonstrating the low systemic toxicity of our scaffolds ([Fig. S8](#)).

Histological H&E staining, TUNEL staining, and immunohistochemical Ki67 staining on different groups of tumor tissues were performed to confirm the anti-tumor recurrence effect ([Fig. 7f](#)). The H&E staining images show that almost no tumor cell apoptosis was observed in the G1, G2, and G3 tumor tissues. Tumor cell apoptosis was observed in varying degrees in G4 and G7 tumor tissue slices, indicating that photothermal treatment alone (even above 50°C) can induce tumor cell apoptosis, but not completely. In contrast, there were more nuclear fragments and lighter cytoplasmic staining in G5 and G6 tumor tissue slices, particularly in G6, indicating that the tumor tissue had undergone degenerative changes following mild photothermal-chemotherapy. The TUNEL images show that G6 tumor tissue slices exhibited remarkable antitumor effects from the largest area of apoptotic tumor cells identified in

brown. Similarly, the Ki67 level was the lowest in the G6 tumor tissue slices, and a large area of cells was stained blue, showing that the mild photothermal-chemotherapy suppressed tumor cell proliferation and boosted antitumor activity. The mechanism of mild photothermal therapy was examined at the protein level using immunofluorescence labeling of HSP70. In comparison to G1, G2, and G3 (without laser irradiation), HSP70 expression was elevated in tumor cells of G4, G5, and G7 after laser irradiations, notably in G7 with high temperature. HSP70 expression in G6 was lower than in G4, G5, and G7, which was due to the loading and release of the HSP70 inhibitor Az. These results demonstrate that mild photothermal-chemotherapy can dramatically cause tumor cell death and limit tumor recurrence.

Furthermore, the histological characteristics of skin tissues around G1, G6, and G7 lesions were analyzed by H&E staining to further investigate the impact of laser irradiation and temperature modulation of PCF scaffolds on normal tissue surrounding lesions [47]. As illustrated in [Fig. 7g](#), there is no evident damage to the skin tissue in G1, and the entire skin tissue structure, including the skin layer (red arrows), hair follicles (yellow arrows), and fat cells (green arrows), is represented. The skin tissue surrounding the G6 and G7 lesions was thermally damaged to varied degrees. The higher photothermal temperature clearly damaged the skin tissue in G7, leaving no epidermis or dermis. In G7, the injured skin tissue measured 4144.8 μm (blue dotted arrow). In contrast, due to the PCF scaffold's ability to regulate temperature, G6 skin tissue damage is minimal (with a size of approximately 2557.8 μm), and there are still fat cells and a section of dermal tissue in H&E staining image.

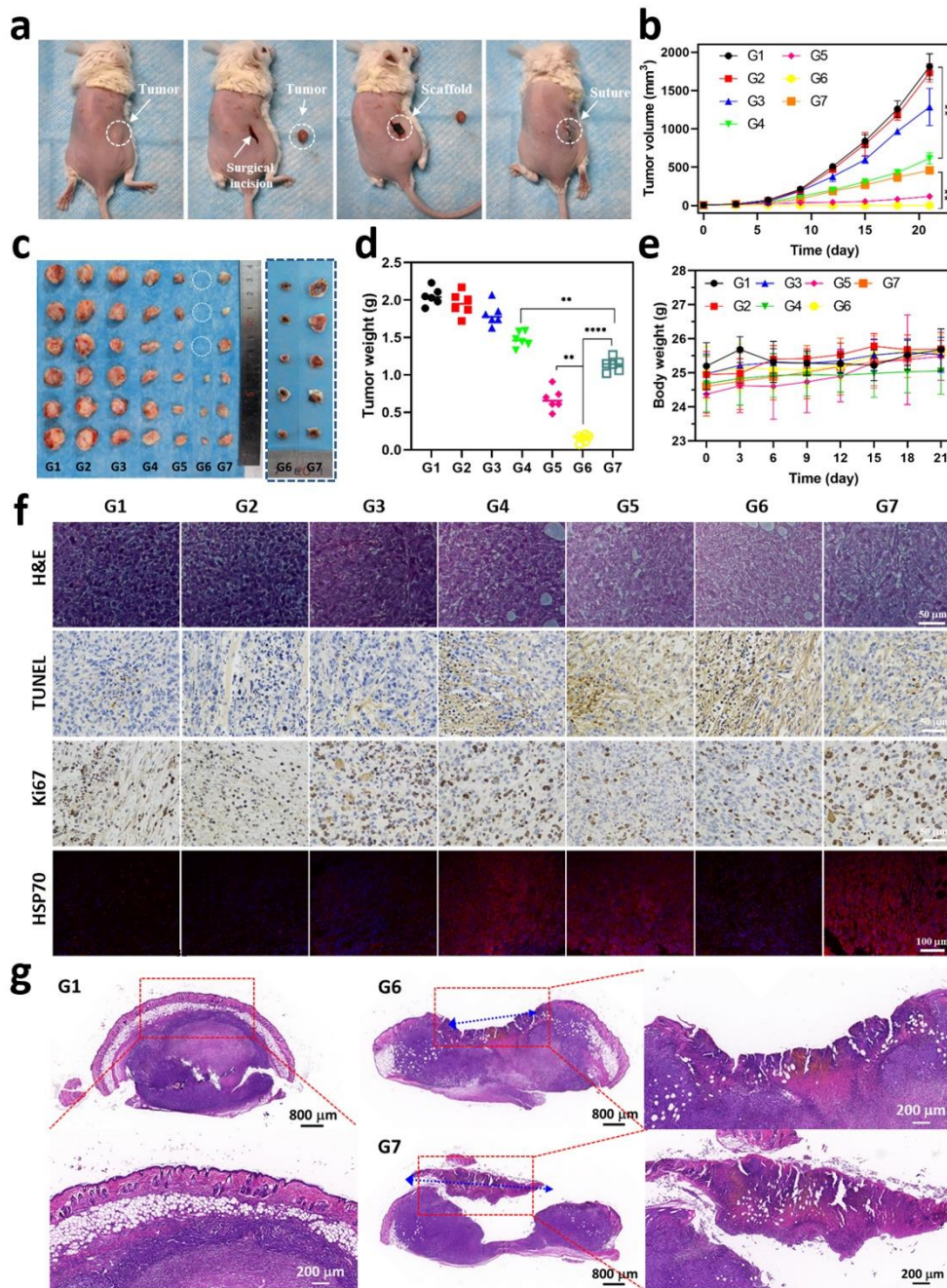


Fig. 7 *In vivo* anti-tumor and thermal damage mitigation effect. **a** Surgical and implantation process; **b** Volume change of the recurrent tumor; **c** Photographic images of excised tumors and skin tissues; **d** Tumor weight; **e** Body weight; **f** H&E staining images, TUNEL staining images, Ki67 staining images, HSP70 expression of tumor tissue slices; **g** H&E staining images of skin tissues of G1, G6 and G7. The data are shown as mean \pm SD (n = 6), P < 0.05 (*), P < 0.01 (**), and P < 0.001 (***)

4. Conclusions

In conclusion, a temperature-regulating PCF-based scaffold has been designed that combines mild photothermal and chemotherapy for tumor recurrence prevention and thermal damage mitigation. By loading LA, DOX, and Az into HCFs, a PCF/DOX/Az scaffold with excellent photothermal conversion capacity, high latent heat (151.5 J/g), and drug loading capacity was fabricated. Under laser irradiation, the prepared PCF-based composite scaffolds act as a thermal trigger for temperature regulation and controlled drug release. In comparison to using third-party instruments to detect the temperature of photothermal therapy [8, 47], this study demonstrated active and effective temperature regulation of the lesion site through the treatment with our fibrous scaffold. Both *in vitro* and *in vivo* results confirmed that the PCF/DOX/Az scaffold significantly improves anticancer efficacy while reducing damage to healthy tissue cells. Overall, this new type of PCF-based composite scaffold offers a promising alternative for local temperature regulation and controlled drug release in mild photothermal-chemotherapy. This PCF-based scaffold could be investigated in further studies to widen the use of temperature regulating systems in cooperative treatment and intelligent drug delivery.

Conflicts of interest

The authors declare that they have no known competing financial interests or personal relationships that could have appeared to influence the work reported in this paper.

Acknowledgements

The authors thank the financial support from National Key R&D Program of China (No. 2017YFC1105003, 2021YFB3802700), National Natural Science Foundation of China (No. 21807046), Guangdong Project (No. 2016ZT06C322), National Natural Science Foundation of Guangdong (No. 2020A151501744), Science and Technology Program of Guangzhou (No. 202102020759), Guangdong Basic and Applied Basic Research Foundation (No. 2021A151511174), and Overseas Expertise Introduction Center for Discipline Innovation (“111 Center”).

Appendix A. Supplementary data

Supplementary data related to this article can be found at

Notes and references:

1. Sung H, Ferlay J, Siegel RL, Laversanne M, Soerjomataram I, Jemal A, Bray F. Global cancer statistics 2020: Globocan estimates of incidence and mortality worldwide for 36 cancers in 185 countries. *CA Cancer J. Clin.* **2021**, *71*: 209.
2. Melamed JR, Edelstein RS, Day ES. Elucidating the fundamental mechanisms of cell death triggered by photothermal therapy. *ACS Nano* **2015**, *9*: 6.
3. Vines JB, Yoon JH, Ryu NE, Lim DJ, Park H. Gold nanoparticles for photothermal cancer therapy. *Front. Chem.* **2019**, *7*: 167.
4. Chen L, Yu QQ, Cheng K, Topham PD, Xu MM, Sun XQ, Pan YM, Jia YF, Wang S, Wang LG. Can photothermal post-operative cancer treatment be induced by a thermal trigger? *ACS Appl. Mater. Interfaces.* **2021**, *13*: 60837.
5. Zhi D, Yang T, O'hagan J, Zhang S, Donnelly RF. Photothermal therapy. *J. Control. Release.* **2020**, *325*: 52.
6. Zhao P, Jin Z, Chen Q, Yang T, Chen D, Meng J, Lu X, Gu Z, He Q. Local generation of hydrogen for enhanced photothermal therapy. *Nat. Commun.* **2018**, *9*: 1.

7. Gao P, Wang H, Cheng Y. Strategies for efficient photothermal therapy at mild temperatures: Progresses and challenges. *Chin. Chem. Lett.* **2022**, *33*: 575.
8. Zhu X, Feng W, Chang J, Tan YW, Li J, Chen M, Sun Y, Li F. Temperature-feedback upconversion nanocomposite for accurate photothermal therapy at facile temperature. *Nat. Commun.* **2016**, *7*: 1.
9. Zhen X, Xie C, Pu K. Temperature-correlated afterglow of a semiconducting polymer nanococktail for imaging-guided photothermal therapy. *Angew. Chem. Int. Ed.* **2018**, *130*: 4002.
10. Shen S, Feng L, Qi S, Cao J, Ge Y, Wu L, Wang S. Reversible thermochromic nanoparticles composed of a eutectic mixture for temperature-controlled photothermal therapy. *Nano Lett.* **2020**, *20*: 2137.
11. Sharma A, Tyagi VV, Chen C, Buddhi D. Review on thermal energy storage with phase change materials and applications. *Renew. Sust. Energ. Rev.* **2009**, *13*: 318.
12. Pielichowska K, Pielichowski K. Phase change materials for thermal energy storage. *Prog. Mater. Sci.* **2014**, *65*: 67.
13. Shchukina E, Graham M, Zheng Z, Shchukin D. Nanoencapsulation of phase change materials for advanced thermal energy storage systems. *Chem. Soc. Rev.* **2018**, *47*: 4156.
14. Yu CH, Wang TR, Wei H, Diao H C, Liu N, Zhang Y, Jiang H Y, Zhao P, Shan Z Y, Sun ZW, Wu T, Mo XM, Yu TB. Photothermal-triggered structural change of nanofiber scaffold integrating with graded mineralization to promote tendon-bone healing. *Adv. Fiber Mater.* **2022**, 1-15.
15. Hasan A, Sayigh A. Some fatty acids as phase-change thermal energy storage materials. *Renew. Energ.* **1994**, *4*: 69.
16. Dai Y, Su J, Wu K, Ma W, Wang B, Li M, Sun P, Shen Q, Wang Q, Fan Q. Multifunctional thermosensitive liposomes based on natural phase-change material: Near-infrared light-triggered drug release and multimodal imaging-guided cancer combination therapy. *ACS Appl. Mater. Interfaces.* **2019**, *11*: 10540.
17. Agarwal S, Greiner A, Wendorff J H. Functional materials by electrospinning of polymers. *Prog. Polym. Sci.* **2013**, *38*: 963.
18. Chen L, Wang S, Yu QQ, Topham PD, Chen CZ, Wang LG. A comprehensive review of electrospinning block copolymers. *Soft Matter* **2019**, *15*: 2490.
19. Chen C, Wang LG, Huang Y. A novel shape-stabilized PCM: Electrospun ultrafine fibers based on lauric acid/polyethylene terephthalate composite. *Mater. Lett.* **2008**, *62*: 3515.
20. Wu Y, Chen CZ, Jia YF, Wu J, Huang Y, Wang LG. Review on electrospun ultrafine phase change fibers (PCFs) for thermal energy storage. *Appl. Energ.* **2018**, *210*: 167.
21. Yu N, Wang ZJ, Zhang JL, Liu ZX, Zhu B, Yu J, Zhu MF, Peng C, Chen ZG. Thiol-capped Bi nanoparticles as stable and all-in-one type theranostic nanoagents for tumor imaging and thermoradiotherapy. *Biomaterials* **2018**, *161*: 279-291.
22. Yu N, Qiu P, Ren Q, Wen M, Geng P, Macharia DK, Zhu MF, Chen ZG. Transforming a sword into a knife: persistent phototoxicity inhibition and alternative

therapeutical activation of highly-photosensitive phytochlorin. *ACS Nano* **2021**, *15*: 19793-19805.

23. Yu N, Tu WZ, Qiu P, Ren Q, Chen XM, Zhu MF, Liu Y, Chen ZG. Full-route advances via biomimetic and biodegradable ultrasmall-in-nano architectures with radiation-photo synergy. *Nano Today* **2022**, *43*: 101427.

24. Chang M, Hou Z, Wang M, Yang C, Wang R, Li F, Liu D, Peng T, Li C, Lin J. Single-atom pd nanozyme for ferroptosis-boosted mild-temperature photothermal therapy. *Angew. Chem. Int. Ed.* **2021**, *133*: 13081.

25. Chang X, Zhang M, Wang C, Zhang J, Wu H, Yang S. Graphene oxide/bahof5/peg nanocomposite for dual-modal imaging and heat shock protein inhibitor-sensitized tumor photothermal therapy. *Carbon* **2020**, *158*: 372.

26. Ali MR, Ali HR, Rankin C R, El-Sayed M. Targeting heat shock protein 70 using gold nanorods enhances cancer cell apoptosis in low dose plasmonic photothermal therapy. *Biomaterials* **2016**, *102*: 1.

27. Xue Y, Wang Y, An J, Sedgwick A, Li M, Xie J, Hu W, Kang J, Sen S, Steinbrueck A, Zhang B, Qiao L, Wageh S, Arambula J, Liu L, Zhang H, Sessler J, Kim J. 2D-ultrathin MXene/DOXjade platform for iron chelation chemo-photothermal therapy. *Bioact. Mater.* **2022**, *14*: 76.

28. Huang H, Yuan G, Xu Y, Gao Y, Mao Q, Zhang Y, Bai L, Li W, Wu A, Hu W, Pan Y, Zhou G. Photoacoustic and magnetic resonance imaging-based gene and photothermal therapy using mesoporous nanoagents. *Bioact. Mater.* **2022**, *9*:157.

29. Krukiewicz K, Zak J K. Biomaterial-based regional chemotherapy: Local anticancer drug delivery to enhance chemotherapy and minimize its side-effects. *Mater. Sci. Eng. C.* **2016**, *62*: 927.

30. Cui X, Liang Z, Lu J, Wang X, Jia F, Hu Q, Xiao X, Deng X, Wu Y, Sheng W. A multifunctional nanodiamond-based nanoplatform for the enhanced mild-temperature photothermal/chemo combination therapy of triple negative breast cancer via an autophagy regulation strategy. *Nanoscale* **2021**, *13*: 13375.

31. Ni JS, Zhang X, Yang G, Kang T, Lin X, Zha M, Li Y, Wang L, Li K. A photoinduced nonadiabatic decay-guided molecular motor triggers effective photothermal conversion for cancer therapy. *Angew. Chem. Int. Ed.* **2020**, *132*: 11394.

32. Bye FJ, Wang LG, Bullock AJ, Blackwood KA, Ryan AJ, MacNeil S. Postproduction processing of electrospun fibres for tissue engineering. *JoVE (J. Vis. Exp.)* **2012**, *66*: e4172.

33. Sun J, Jiang H, Zhao C, Fan X, Chao C, Zhao T. Holey aligned electrodes through in-situ ZIF-8-assisted-etching for high-performance aqueous redox flow batteries. *Sci. Bull.* **2021**, *66*: 904.

34. Wang C, Zheng T, Luo R, Liu , Zhang M., Li J, Sun X, Shen , Han W, Wang L. In situ growth of zif-8 on pan fibrous filters for highly efficient u (vi) removal. *ACS Appl. Mater. Interfaces.* **2018**, *10*: 24164.

35. Wu S, Ma X, Peng D, Bi Y. The phase change property of lauric acid confined in carbon nanotubes as nano-encapsulated phase change materials. *J. Therm. Anal. Calorim.* **2019**, *136*: 2353.

36. Shamsaei E, Basquiroto de Souza F, Fouladi A, Sagoe-Crentsil K, Duan W. Graphene oxide-based mesoporous calcium silicate hydrate sandwich-like structure: Synthesis and application for thermal energy storage. *ACS Appl. Energy Mater.* **2022**, 5: 958.
37. Qi G, Yang J, Bao R, Xia D, Cao M, Yang W, Yang M, Wei D. Hierarchical graphene foam-based phase change materials with enhanced thermal conductivity and shape stability for efficient solar-to-thermal energy conversion and storage. *Nano Res.* **2017**, 10: 802.
38. Choi SW, Zhang Y, Xia Y. A temperature-sensitive drug release system based on phase-change materials. *Angew. Chem. Int. Ed.* **2010**, 49: 7904.
39. Abdalkarim SYH, Yu H, Wang C, Chen Y, Zou Z, Han L, Yao J, Tam KC. Thermo and light-responsive phase change nanofibers with high energy storage efficiency for energy storage and thermally regulated on-off drug release devices. *Chem. Eng. J.* **2019**, 375: 121979.
40. Jin Z. About the evaluation of drug combination. *Acta Pharmacol. Sin.* **2004**, 25: 146.
41. Chen L, Yu QQ, Jia YF, Xu MM, Wang YY, Wang J, Wen T, Wang LG. Micro-and-nanometer topological gradient of block copolymer fibrous scaffolds towards region-specific cell regulation. *J. Colloid Interf. Sci.* **2022**, 606: 248.
42. Li X, Xu F, He Y, Li Y, Hou J, Yang G, Zhou S. A hierarchical structured ultrafine fiber device for preventing postoperative recurrence and metastasis of breast cancer. *Adv. Funct. Mater.* **2020**, 30: 2004851.
43. Zhao J, Cui W. Functional electrospun fibers for local therapy of cancer. *Adv. Fiber Mater.* **2020**, 2: 229.
44. Chen L, Zhang D, Cheng K, Li WC, Yu QQ, Wang LG. Photothermal-responsive fibrous dressing with enhanced antibacterial activity and cell manipulation towards promoting wound-healing. *J. Colloid Interf. Sci.* **2022**, 623: 21.
45. Niu W, Guo Y, Xue Y, Wang M, Chen M, Winston DD, Cheng W, Lei B J. Biodegradable multifunctional bioactive eu-gd-si-ca glass nanoplatfrom for integrative imaging-targeted tumor therapy-recurrence inhibition-tissue repair. *Nano Today* **2021**, 38: 101137.
46. Wang H, Xu S, Fan D, Geng X, Zhi G, Wu D, Shen H, Yang F, Zhou X, Wang X. Multifunctional microcapsules: A theranostic agent for US/MR/PAT multi-modality imaging and synergistic chemo-photothermal osteosarcoma therapy. *Bioact. Mater.* **2022**, 7: 453.
47. Ma L, Zhou Y, Zhang Z, Liu Y, Zhai D, Zhuang H, Li Q, Yuye J, Wu C, Chang J. Multifunctional bioactive Nd-Ca-Si glasses for fluorescence thermometry, photothermal therapy, and burn tissue repair. *Sci. Adv.* **2020**, 6: eabb1311.